Silicon photonics-based high-energy passively *Q*-switched laser

Neetesh Singh [1] ✉**, Jan Lorenzen** [1,2]**, Milan Sinobad** [1]**, Kai Wang** [3]**,
Andreas C. Liapis** [4]**, Henry C. Frankis**[5]**, Stefanie Haugg** [6]**, Henry Francis**[7]**,
Jose Carreira**[7]**, Michael Geiselmann**[7]**, Mahmoud A. Gaafar**[1]**, Tobias Herr** [1,8]**,
Jonathan D. B. Bradley**[5]**, Zhipei Sun** [4]**, Sonia M. Garcia-Blanco**[3] **&
Franz X. Kärtner** [1,8]

Chip-scale, high-energy optical pulse generation is becoming increasingly important as integrated optics expands into space and medical applications where miniaturization is needed. *Q*-switching of the laser cavity was historically the first technique to generate high-energy pulses, and typically such systems are in the realm of large bench-top solid-state lasers and fibre lasers, especially in the long wavelength range >1.8 μm, thanks to their large energy storage capacity. However, in integrated photonics, the very property of tight mode confinement that enables a small form factor becomes an impediment to high-energy applications owing to small optical mode cross-sections. Here we demonstrate a high-energy silicon photonics-based passively *Q*-switched laser with a compact footprint using a rare-earth gain-based large-mode-area waveguide. We demonstrate high on-chip output pulse energies of >150 nJ and 250 ns pulse duration in a single transverse fundamental mode in the retina-safe spectral region (1.9 μm), with a slope efficiency of ~40% in a footprint of ~9 mm². The high-energy pulse generation demonstrated in this work is comparable to or in many cases exceeds that of *Q*-switched fibre lasers. This bodes well for field applications in medicine and space.

Soon after the invention of the laser, the 'giant pulse' laser was experimentally demonstrated by McClung and Hellwarth[1]. Ever since its invention, *Q*-switching has remained a common technique for generating pulses of very high energy, which have found ample applications in ranging, sensing, micromachining and medicine among others[2–11]. The retina-safe spectral window of extended-short-wave infrared (>1.7 μm) is used in important applications such as laser surgery, biological imaging, food and environmental monitoring, spectroscopy, free-space communications and even recently envisaged local area networks (where fibre loss is acceptable)[12–16]. As an example, *Q*-switched lasers

in this spectral window are specifically used in laser surgery for precise cutting of biological tissues and bone, such as in ophthalmic or spinal surgery and lithotripsy[5–8]. They are also used in the food, semiconductor and electronics industries for humidity control and in differential absorption light detection and ranging (LIDAR) for mapping wind, water and carbon dioxide in the atmosphere[10–12].

Currently, solid-state and fibre lasers are the most dominant technologies that provide the desired power and energy, thanks to their large energy storage capacity due to large signal mode area and long cavity length (mode area × length). Here, large mode area (LMA) is

[1]Center for Free-Electron Laser Science, Deutsches Elektronen-Synchrotron DESY, Hamburg, Germany. [2]University of Kiel, Kiel, Germany. [3]Integrated Optical Systems, MESA+ Institute for Nanotechnology, University of Twente, Enschede, the Netherlands. [4]Department of Electronics and Nanoengineering, Aalto University, Espoo, Finland. [5]Department of Engineering Physics, McMaster University, Hamilton, Ontario, Canada. [6]Center for Hybrid Nanostructures, Universität Hamburg, Hamburg, Germany. [7]LIGENTEC SA, 1024, Ecublens, Switzerland. [8]Department of Physics, Universität Hamburg, Hamburg, Germany. ✉e-mail: neetesh.singh@desy.de

beneficial because (1) it reduces the instability caused by optical non-linearities owing to high intensity and, more importantly, (2) it helps to increase the stored energy and the signal power while increasing the gain saturation power (given by $P_{sat} = E_{sat}/\tau_1$, where τ_1 is the upper-state lifetime and E_{sat} is the saturation energy of the gain medium, which is proportional to the mode area: $E_{sat} \propto A_{eff}$). Therefore, a high-power fibre laser typically employs an LMA fibre to reach the power and energy levels usually enjoyed by solid-state lasers[17,18]. Achieving such a capability on the chip scale will have a disruptive impact in point-of-care and field-deployable systems such as space-bound instruments for earth and planetary LIDARs where size, weight and power are critical[10–12]. In integrated photonics[19–22], the energy storage capacity is severely limited compared with its benchtop counterpart. This is because the cavity length and the mode area are usually limited to around a few centimetres (with reasonable loss) and a few micrometres squared, respectively. Recently, this limitation has been somewhat relaxed by the fabrication of low-loss long (50 cm) silicon nitride (SiN) waveguides allowing high signal amplification[23]. However, that is at the cost of a challenging fabrication process, and the high optical nonlinearity in such long waveguides is a cause of concern. On the other hand, semiconductor gain media can achieve very high gain over a short length owing to their large emission cross-sections[24,25]. However, semiconductor gain media have poor energy storage capability owing to their short upper-state lifetime and high nonlinear losses such as two-photon absorption. Nevertheless, progress has been made with continuous wave (CW) lasers such as those based on gallium antimonide operating at around 1.9 µm. They have been demonstrated to produce a few milliwatts of power[26,27], and LMA structures are also being investigated (currently for 1.55 µm) for integration with silicon photonics[28,29].

In this Article, we demonstrate high-energy pulse generation from a chip-scale device with a performance level comparable to and in many cases surpassing that of fibre lasers. This was enabled by LMA waveguides[30] that support a mode area of several tens of micrometres squared while allowing for a long cavity within a compact footprint[31,32]. Although the device was not fabricated in a standard complementary metal oxide semiconductor (CMOS) foundry, the fabrication process used here is CMOS compatible and the device can be co-integrated in the future with electronics using emerging multichip 3D/2.5D co-integration techniques[33,34]. Our LMA design is based on a single thick silicon nitride layer that allows for tight bends for a compact footprint (and also for seamless integration of conventional nonlinear photonics components[35]). The thickness of the SiN layer can vary depending on the wavelength and the foundry process, which simplifies the fabrication and allows for adaptation to different CMOS foundries. In comparison, the design used in refs. 36–38 was based on multiple SiN layers for transitioning between passive and gain layers, which may cause internal parasitic reflections and loss at the transitions[39], which is eliminated here. Moreover, the gain waveguide only supported a small mode area (and thus low gain saturation energy) and was weakly multimode. Our LMA design supports only fundamental mode propagation and allows high pump and signal mode overlap even when they are spectrally far apart[30–32], unlike an LMA fibre. Since the optical modes are mainly guided in the gain film, the gain waveguide propagation loss is determined by the film loss, which is intrinsically lower than that of an etched waveguide[40,41]. Using the LMA waveguide and rare-earth gain medium[41–54], we demonstrate a Q-switched high-energy laser achieving pulse energies over 150 nJ (with a pulse width of 250 ns) around 1.9 µm within a device footprint of ~9 mm². The Q-switched pulse energy demonstrated here is ~20 dB higher, and the slope efficiency is ~40% as compared with 1% in the previous demonstration[36]. More importantly, the pulse energy, average power and slope efficiency are higher than those of many benchtop true saturable absorber-based Q-switched all-fibre lasers[55–63] (see Supplementary Information for a comparison). Pulses with even higher peak power and shorter duration can be achieved, provided that we operate below the optical damage threshold of the SiN waveguide[64–66].

Integrated Q-switched laser

For decades, Q-switching has been the technique to generate highly energetic pulses from a laser by modulating the loss and thus the quality factor (Q) of the cavity. When the Q of the cavity is low, that is, when stimulated emission is suppressed, the pump excites the gain ions to upper states, storing energy until a high population inversion is achieved. A sudden change of Q to a high state (by reducing the loss) allows stimulated emission to take place, causing an instantaneous conversion of stored energy in the gain medium into signal photons and a rapid build-up of a high-power circulating signal. In doing so, the high intracavity power depletes the gain, causing signal amplification to cease as soon as the gain drops below the cavity loss, which results in the emission of a giant pulse from the cavity. A cartoon showing this process is shown in Fig. 1a. Switching of the cavity Q can be attained actively or passively. Active Q-switching requires an externally controlled intracavity modulator such as an electro-optic device, which makes the system complex and bulky. Passive Q-switching, on the other hand, requires a saturable absorber whose loss drops with pulse intensity or energy and which is a cost-effective, compact and robust component. For this reason, there is a strong desire in the fibre community to develop passively Q-switched high energy lasers, and several groups have tried different types of saturable absorbers over the past decade that are durable and inexpensive, have a high damage threshold and are compact[55–63,67–71]. In the integrated passively Q-switched laser presented here, we utilize an artificial saturable absorber that is durable and has a high damage threshold, limited only by the damage threshold of the SiN waveguides[30,37,64].

The laser mainly consists of a gain section, cavity mirrors and a saturable absorber (Fig. 1b). The pump is coupled to the gain section through an integrated wavelength division multiplexer (WDM), which in reverse guides the signal to an integrated loop mirror reflector. The pump is adiabatically coupled into the gain medium, which is based on thulium-doped aluminium oxide film (~840 nm thick), which is cladded with a 1-µm-thick silica layer. The cross-section of the LMA gain waveguide is shown along with the simulated fundamental transverse electric mode profile of the signal in Fig. 1b (inset). The signal mode area is 26.7 µm², and the pump mode area is 26.3 µm², resulting in a pump and signal mode overlap of >99%. The thickness (h) and width (w) of the SiN layer in the gain section are 800 nm and 290 nm, respectively, and the interlayer oxide thickness (g) is 300 nm. The power overlap factors of the signal mode are ~75% in the aluminium oxide gain film, 0.2% in the SiN layer and 11.8% and 13% in the top and the bottom silica layers, respectively. A narrow SiN layer not only reduces scattering loss (owing to a weak modal confinement) but also helps to maintain only the fundamental mode in the gain section. The pump and signal are coupled efficiently into the large fundamental transverse electric mode in the gain section with adiabatic tapers. The tapers also help to pull the large modes back into the SiN layer to allow for tight bends[30]. To obtain a long cavity while keeping the footprint small, we use a serpentine-shaped gain waveguide with circular bends (Fig. 1b). The total cavity round-trip length is 16.7 cm, which includes a 12 cm round-trip length of the gain section. Near the output end of the gain section, the signal is adiabatically coupled into a wide SiN waveguide, which leads to the integrated saturable absorber. We use a fast Kerr-type saturable absorber based on a nonlinear Michelson interferometer-based saturable absorber (NLI-SA)[30,37]. It acts as an intensity-dependent reflector: the reflectivity back to the cavity increases with the signal intensity, which supports the Q-switched pulse formation (for details, see ref. 30).

The NLI-SA consists of a non-3dB coupler and two symmetric arms terminated with loop mirrors. The non-3dB coupler splits the signal into the two arms with different power levels. Therefore, by propagating in the nonlinear waveguides, the modes acquire a power-dependent
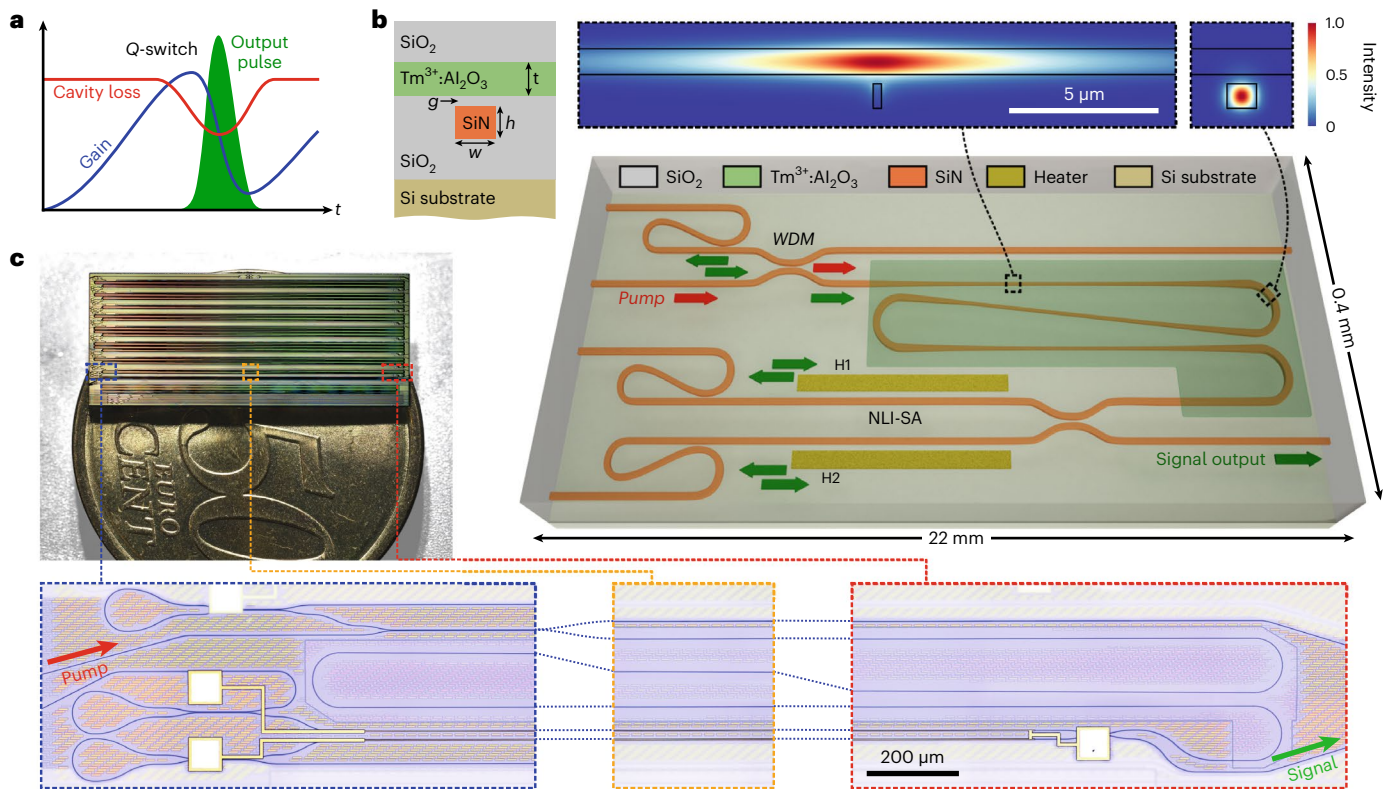
Fig. 1 | Principle of passive *Q*-switching and the intergrated *Q*-switched laser.
a, The principle of passive *Q*-switching. **b**, A compact integrated LMA pulsed laser. WDM, wavelength division multiplexer; NLI-SA, nonlinear Michelson interferometer-based saturable absorber; H1 and H2, high- and low-power heater arms. The pump is coupled into the gain section through a WDM. Within the green box region, the LMA sections are over the straight SiN waveguides, which are connected with each other through adiabatic tapers and tight bends. The NLI-SA splits the signal into two arms through a directional coupler and back-reflects via loop mirrors. Inset, the LMA waveguide cross-section along with the signal mode profiles in an LMA gain region and a bend. **c**, An optical image of the chip containing the device placed on top of a 50 cent Euro coin. Owing to the large aspect ratio of the device, for clarity microscope images were taken at different regions (dashed lines connecting these images are simply guides to the eye).

Kerr phase shift difference with respect to each other. This in turn affects the reflectivity of the NLI-SA, which increases with the signal power until a π phase difference allows for maximum signal reflection back to the cavity.

Results

The passive layer of the device was fabricated in a silicon photonics foundry (Ligentec). A thick SiN layer is deposited, polished, patterned and subsequently cladded with a silica layer. A local oxide opening is created where the silica layer is etched away, leaving only ~300 nm (*g*) above the SiN layer, and subsequently a gain layer is deposited (Fig. 1b, green box). For the gain deposition, a 840-nm-thick thulium-doped alumina gain layer ($Tm^{3+}:Al_2O_3$) is deposited by radio-frequency (RF) sputtering with an estimated thulium ion concentration of 3.2×10^{20} cm^{-3}. The passive film loss is measured separately with the prism coupling technique (Metricon) to be 0.83 dB cm^{-1} at 450 nm and 0.55 dB cm^{-1} at 520 nm, which corresponds to a loss <0.1 dB cm^{-1} beyond 1.55 μm as measured in refs. 40,41. The refractive index of the film was estimated with Sellmeier fitting at 1.9 μm to be 1.70 using an ellipsometer (Supplementary Information). In the gain section, the bend loss is measured to be less than −0.0008 dB per 180° for the bend radius of 90 μm. The broadband spectral response of the passive components is measured with a supercontinuum source (NKT). The WDM has a bandwidth of 130 nm (at the 1 dB level) around the signal at 1.89 μm, and the pump port at 1.61 μm has >90% transmission. The measured 3 dB crossing point of the cross and through port of the directional coupler of the loop mirrors is centred at ~1.89 μm, giving an estimated

reflection bandwidth of 170 nm (at the 1 dB level). The power splitter (a directional coupler) of the NLI-SA has a splitting ratio of 80:20 at the wavelength of 1.9 μm, which results in a modulation depth of >50% for the saturable absorber. Heaters are integrated to compensate for fabrication uncertainties, that is, to properly bias the NLI-SA to compensate for the phase offset between the two arms caused by fabrication tolerances, and to vary the self-amplitude modulation parameter of the NLI-SA. The bias of the NLI-SA is a key parameter to control the mode of operation of the laser (that is, pulsed or CW), as explained below in more detail.

In the experiment, the pump at a wavelength of 1.61 μm is launched into the chip with a lensed fibre. The laser starts to operate in CW mode, and as the pump power increases, inherent relaxation oscillation builds up and passively *Q*-switched high-energy pulses emerge, which is due to the presence of a loss modulator such as a saturable absorber, as mentioned above. The optical spectrum of the signal at 400 mW of coupled pump power in the cavity is shown in Fig. 2a, measured at the output port. The measured slope efficiency of the laser is 40%, and the lasing threshold pump power is around 20 mW (Fig. 2b). The pulses are produced at a repetition rate of <1 MHz with a pulse width of 250 ns and a pulse energy slightly over 150 nJ. The signal is centred at 1.89 μm, which is also around the maximum transmission and reflection wavelength of the pump and signal combiner (WDM) and the loop mirrors, respectively (Supplementary Information). If needed, one can apply a narrow bandpass filter at the output or co-integrate a narrowband filter to extract the narrowband signal around 1,896 nm, which dominates the signal energy (Fig. 2a, linear plot).
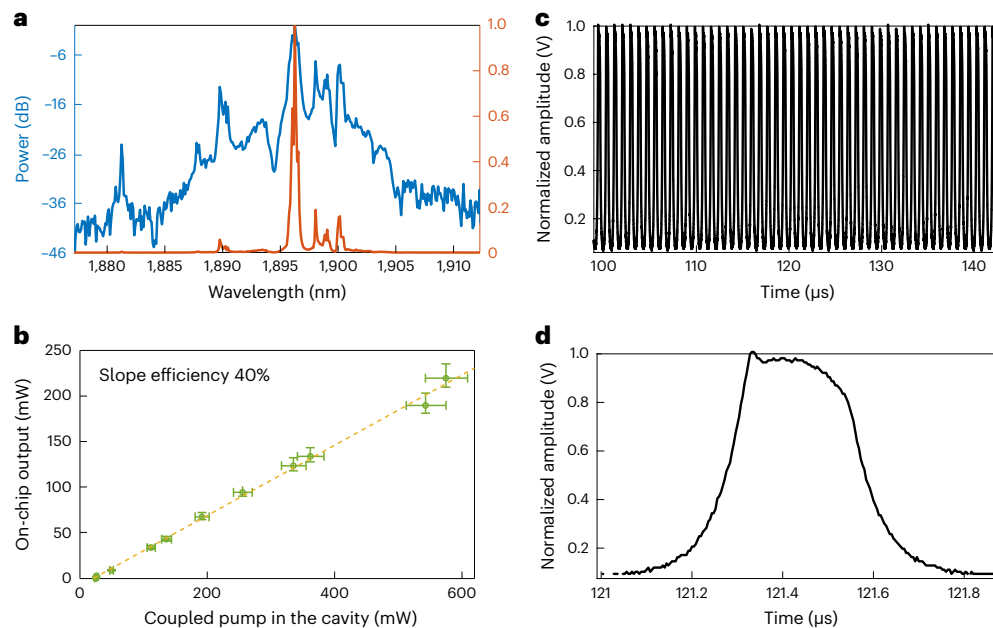
Fig. 2 | Power, spectral and time domain reponse of the laser. a, The optical spectrum on a logarithmic and a linear scale. **b**, The on-chip output signal average power with respect to the on-chip pump power. The error bars denote the uncertainty in power around the mean owing to variations in pump and signal coupling repeated six times. **c**, An oscilloscope trace of the *Q*-switched pulse train. **d**, A zoomed-in section showing a single pulse.
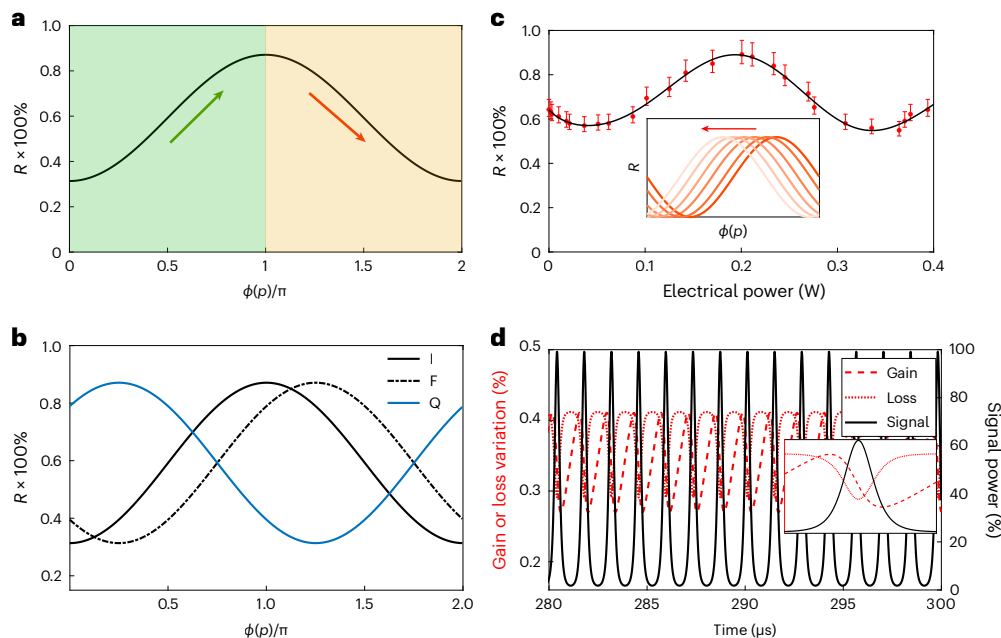

Fig. 3 | Saturable absorber response and laser simulation. a, An ideal reflectivity (*R*) curve of the NLI-SA as a function of the power-dependent differential phase shift. The green and red arrows indicate the pulsed operation region (positive slope) and CW operation region (negative slope), respectively. **b**, The NLI-SA reflectivity curve of an ideal (I), fabricated (F) device and the case where the curve is tuned for *Q*-switching (Q). **c**, A measurement of the thermally tuned NLI-SA reflectivity to help extract the NLI-SA reflectivity curve. The error bars represent the reflectivity variations around the mean for five measurements owing to fluctuations in signal coupling and thermal drift of the chip due to heating. The inset shows a cartoon of how the NLI-SA reflectivity as a function of $\Phi(p)$ shifts with temperature applied by thermal phase shifters, which helps to trace the as-fabricated reflectivity of the NLI-SA (dashed curve in **b**). **d**, The simulated laser dynamics in terms of the cavity round-trip loss, the gain and the output power normalized to its maximum over several periods. Inset, close-up of the dynamics over one pulse.

As mentioned above, owing to fabrication uncertainties, the reflectivity of the as-fabricated NLI-SA is not ideal and can be tuned with an integrated phase shifter to ensure that the signal lies on the positive reflectivity slope of the NLI-SA to allow for pulse formation. The ideal reflectivity curve of the NLI-SA is shown in Fig. 3a. Here, $\Phi(p)$ is the input peak power-dependent nonlinear differential phase shift of the light in the two arms of the interferometer. With a non-3dB splitter, the two arms have different signal power, thus $\Phi(p)$ and the reflectivity back to the cavity increase with the signal power. On the positive slope (increasing reflectivity) in Fig. 3a, the laser cavity tends to form pulses,

such as through *Q*-switching, *Q*-switched mode locking and CW mode locking. In contrast, on the negative slope (decreasing reflectivity), pulse formation is suppressed and the laser operates in the CW mode. With an integrated phase shifter, the NLI-SA can be tuned to switch the laser operation from the CW lasing mode to the pulsed mode. This may find direct applications in laser surgery where the two modes of operation are used, such as CW lasing for neurosurgery and pulsed lasing for spinal surgery[5].

The behaviour of the as-fabricated NLI-SA deviates from the ideal one owing to fabrication uncertainties, causing the reflectivity curve to be shifted (Fig. 3b). One can extract the reflectivity response of the as-fabricated NLI-SA in a laser (Fig. 3c). To this end, we couple a very weak test signal (NKT supercontinuum) in the NLI-SA such that the nonlinear phase shift is negligible ($\Phi(p) \approx 0$) and then gradually increase the thermal phase shift (with an integrated heater), which varies the reflectivity curve, and collect the reflected light, which varies in power (owing to the change in reflectivity). As shown in Fig. 3c (inset), the reflectivity curve is tuned to the left and the reflected power measured near ($\Phi(p) \approx 0$) varies accordingly: first the power drops to a minimum and then increases, whereas in an ideal case it should start by increasing from a minimum. Using this method, we trace out the response of the fabricated NLI-SA (Fig. 3b, dashed curve). We note that the peak-to-peak difference (Fig. 3c) is <40% instead of being larger as expected for a directional coupler with 80:20 splitting ratio at 1.89 µm. This is mainly due to the use of a broadband source causing higher signal reflection from unwanted spectral bands at shorter wavelengths (Supplementary Information). Once the NLI-SA power-dependent reflectivity response has been extracted, it can be shifted either to the right or to the left with respect to the horizontal axis by thermal tuning of the two arms, so that the lasing signal falls on the positive slope of the curve. To obtain *Q*-switched high-energy pulses, the curve was tuned to the right until the reflectivity back to the cavity was increased and the signal fell on the positive slope and not at the peak of the curve (Fig. 3b, blue curve). This results in the generation of a high intracavity signal power and therefore high-energy pulses, which happened around at $\Phi(p) \approx 0.1$, corresponding to an intracavity pulse peak power of ~6–10 W. The curve can also be shifted to the left such that the signal falls near the bottom of the positive slope. However, in that case, the signal reflection back to the cavity is low, which results in lower-energy pulses. We note that, for every pump power, the reflectivity curve of the NLI-SA is slightly readjusted with the heaters such that the signal falls close to the peak reflectivity on the positive slope region. For high-power CW operation, the NLI-SA can be tuned such that the signal lies on the negative slope near the peak of the reflectivity. The thermal cross-talk between the two arms of the NLI-SA is expected to be negligible as they are separated by 30 µm. We simulated the behaviour of the *Q*-switched laser by solving a set of coupled rate equations[72,73] (Supplementary Information), with a modified saturable absorber loss function (a cosine function, to account for the NLI-SA). Since we are operating near the very peak on the positive slope of the NLI-SA reflectivity curve, the effective modulation depth and the saturation power of the saturable absorber are low. This results in a very weak gain and loss modulation, well below 1% (Fig. 3d), causing relatively long pulse formation.

We monitored the stability of the output power of the *Q*-switched laser over several minutes (Fig. 4). The fluctuation is about 1–2%, which is mainly due to the mechanical drift in the alignment of the chip against the input/output lensed fibres. The irregular spacing between the data points is simply due to the manual recording of the data.

Discussion and conclusion

We demonstrated a high-energy *Q*-switched laser in a silicon photonics platform that is CMOS compatible. The laser performance is comparable to, and in many ways exceeds, that of a benchtop fibre laser (Supplementary Table S1). This bodes well for a wide range of applications where size, weight and power are important, such as in deep space and
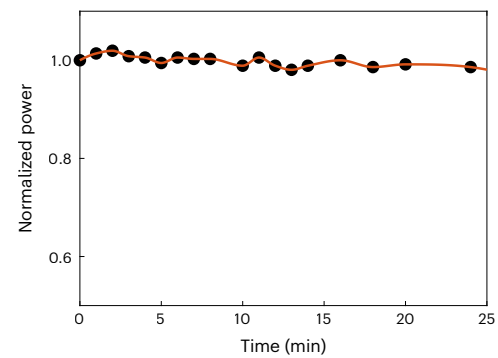

Fig. 4 | Laser power stability. The normalized output power of a *Q*-switched laser over a period of several tens of minutes. The black dots are experimental data and the red curve is a shape-preserving fit to the data.

point-of-care medical applications. For example, *Q*-switched lasers operating beyond >1.8 µm are often used in medical surgery, including urological surgery, lithotripsy (such as kidney stone surgery) and in general as a laser scalpel for soft and hard tissue. Lasers operating at around 2.1 µm, such as a holmium laser, are considered to be the clinical gold standard for laser lithotripsy[6]. Thulium lasers, on the other hand, operate at around 1.9 µm, where the water absorption is even stronger, which helps to reduce the tissue ablation threshold by a factor of four compared with holmium lasers[6]. However, the lasers used in such surgeries (which do not require ultra-high-precision cutting) produce long pulses, several microseconds long, at low repetition rates of several hundreds of hertz[6,74–76], which are delivered to the target with a multimode fibre that often compromises beam quality and therefore intensity. An integrated *Q*-switched laser, such as the one demonstrated in this work, offers pulses with sub-microsecond pulse duration at relatively higher repetition rates as well as high beam quality and intensity at the output. Therefore, an integrated laser offers similar or even better surgical quality compared with a fibre laser, in addition to its lower energy fluence (and thus lower collateral damage), small form factor and low operation cost. Other promising directions for such integrated 'retina-safe' lasers are in time-of-flight sensors such as automotive LIDARs[77] and space applications. Space agencies are interested in reducing the size and weight of next-generation sensing systems such as differential absorption LIDAR for greenhouse gas detection[78,79]. Future satellite and lander/rover missions can be equipped with 1.9 µm lasers for ranging and absorption spectroscopy of molecules essential for life, such as water and ammonia.

The device can be designed to support an even larger mode area than shown in this work, reaching the levels of a fibre laser. This will substantially increase the stored energy, helping the intracavity pulse energy of the signal to reach the several microjoule range. Furthermore, shorter pulses (in the sub-nanosecond range) with high peak power can be extracted by increasing the NLI-SA's saturable loss and saturable power with thermal tuning. However, caution must be exercised to limit the intracavity pulse energy to be within the damage threshold of the SiN waveguides. Damage thresholds of dielectrics scale with the pulse width τ, typically ~$\tau^{0.5}$ for $\tau > 10$ ps durations[65]. Damage threshold energies are particularly low in the regions where the mode is tightly confined, such as in the SiN bends in the gain section. For the current device, the damage threshold is in the range of hundreds of nanojoules to one microjoule (for nanosecond pulses)[64–66]. We have observed damage in our devices, especially in the bends in the gain section close to the NLI-SA after full amplification. To avoid damage of the SiN waveguides while tuning the NLI-SA, monitoring of the laser energy and the pulse duration is necessary to stay below the damage threshold.

The design is scalable to different wavelength windows, such as the 1.55 µm telecommunications window and the 1 µm high-power laser window, by using erbium and ytterbium dopants, respectively.

Many applications need a regular, high repetition rate train of low-noise pulses, for example, frequency combs. To achieve this functionality of the laser, albeit at lower pulse energies, one can also integrate apodised chirped Bragg gratings in place of the loop mirrors to manage the cavity dispersion and favour CW mode locking. Care must be taken, however, to avoid undesired *Q*-switching that may lead to cavity component damage, as discussed above.

Online content

Any methods, additional references, Nature Portfolio reporting summaries, source data, extended data, supplementary information, acknowledgements, peer review information; details of author contributions and competing interests; and statements of data and code availability are available at https://doi.org/10.1038/s41566-024-01388-0.

References

1. McClung, F. J. & Hellwarth, R. E. Giant optical pulsation from ruby. *J. Appl. Phys.* **33**, 828–829 (1962).
2. Sharma, U. et al. Highly stable tunable dual wavelength Q-switched fiber laser for DIAL applications. *IEEE Photonics Tech. Lett.* **16**, 1277–1279 (2004).
3. Nagele, M. et al. Passively Q-switched 914 nm microchip laser for lidar systems. *Opt. Express* **29**, 23799–23809 (2021).
4. Skorczakowski, M. et al. Mid infrared Q switched Er:YAG laser for medical applications. *Laser Phys. Lett.* **7**, 498–504 (2010).
5. Scholle, K, et al. in *Frontiers in Guided Wave Optics and Optoelectronics* (ed. Pal, B.) Ch. 22 (IntechOpen, 2010).
6. Fried, N. M. & Irby, P. B. Advances in laser technology and fibre-optic delivery systems in lithotripsy. *Nat. Rev. Urol.* **15**, 563–573 (2018).
7. Yang, K., Yang, Y., He, J. & Zhao, S. in *Nonlinear Optics - From Solitons to Similaritons* (eds Bakırtaş, İ. & Antar, N.) Ch. 5 (IntechOpen, 2019).
8. Boone, C. Medical applications are a surgical fit for 2 μm lasers. *Lasers & Sources* (2022).
9. Xie, X. et al. A brief review of 2 μm laser scalpel. In *Proc. IEEE 5th Optoelectronics Global Conference* (IEEE, 2022).
10. Singh, U. N. Progress on high-energy 2-micron solid state laser for NASA space-based wind and carbon dioxide measurements. In *Proc. IEEE Photonics Society Summer Topical Meeting Series* (IEEE, 2011).
11. Yu, W. et. al. Orbiting and *in-situ* lidars for earth and planetary applications. *IEEE J. Sel. Top. Appl. Earth Obs. Remote Sens.* https://doi.org/10.1109/JSTARS.2021.3103929 (2021).
12. Guilhot, D. et al. Laser technology in photonic applications for space. *MDPI Photonics Dev. Appl.* **3**, 50 (2019).
13. Bruns, O. T. et al. Next-generation in vivo optical imaging with short-wave infrared quantum dots. *Nature. Biomed. Eng.* **1**, 0056 (2017).
14. Kakouta, N. et al. Near-infrared imaging of water vapour in air. *Meas. Sci. Technol.* **33**, 075403 (2022).
15. Hodgkinson, J. et al. Optical gas sensing: a review. *Meas. Sci. Technol.* **24**, 012004 (2013).
16. Li, Z. et al. Thulium-doped fiber amplifier for optical communications at 2 μm. *Opt. Express* **21**, 9289 (2013).
17. Renaud, C. C. et al. Characteristics of Q-switched cladding-pumped ytterbium-doped fiber lasers with different high-energy fiber designs. *IEEE J. Quantum Electron.* **37**, 199–206 (2001).
18. Richardson, D. J. et al. High power fiber lasers: current status and future perspectives. *J. Opt. Soc. Am. B* **27**, B63–B92 (2010).
19. Zhou, Z. et al. On-chip light sources for silicon photonics. *Light: Sci. Appl.* **5**, e358 (2015).
20. Chang, L. et al. Integrated optical frequency comb technologies. *Nat. Photonics* **16**, 95–108 (2022).
21. Hermanns, A. et al. High-pulse-energy III–V-on-silicon-nitride mode-locked laser. *APL Photonics* **6**, 096102 (2021).
22. Davenport, M. L. et al. Integrated heterogeneous silicon/III–V mode-locked lasers. *Photonics Res.* **6**, 468–478 (2018).
23. Liu, Y. et al. A photonic integrated circuit based erbium doped amplifier. *Science* **376**, 1309–1313 (2022).
24. Leuthold, J. et al. Material gain of bulk 1.55 mm InGaAsP/InP semiconductor optical amplifiers approximated by a polynomial model. *J. Appl. Phys* **87**, 618–620 (2000).
25. Geskus, D. et al. Giant optical gain in a rare-earth-ion-doped microstructure. *Adv. Mater.* **24**, 19–22 (2012).
26. Wang, R. et al. Compact GaSb/silicon-on-insulator 2.0x μm widely tunable external cavity lasers. *Opt. Express* **24**, 28977–28986 (2016).
27. Zia, N. et al. Hybrid silicon photonics DBR laser based on flip-chip integration of GaSb amplifiers and μm-scale SOI waveguides. *Opt. Express* **30**, 24995–25005 (2022).
28. Zhao, H. et al. High power indium phosphide photonic integrated circuits. *IEEE J. Sel. Top. Quantum Electron.* **25**, 1–10 (2019).
29. Juodawlkis, P. W. et al. High-power, low-noise 1.5-μm slab-coupled optical waveguide (SCOW) emitters: physics, devices, and applications. *IEEE J. Sel. Top. Quantum Electron.* **17**, 1698–1714 (2011).
30. Singh, N. et al. Towards CW modelocked laser on chip – a large mode area and NLI for stretched pulse mode locking. *Opt. Express* **28**, 22562–22579 (2020).
31. Singh, N. et al. Large mode area waveguide for silicon photonics and modelocked lasers. In *Proc. Conference on Lasers and Electro-Optics* (Optica Publishing Group, 2022).
32. Singh, N. et al. Towards CMOS compatible high power mode-locked lasers and frequency combs. In *Proc. Conference on Lasers and Electro-Optics* (Optica Publishing Group, 2022).
33. Margalit, N. et al. Perspective on the future of silicon photonics and electronics. *Appl. Phys. Lett.* **118**, 220501 (2021).
34. Ranno, L. et al. Integrated photonics packaging: challenges and opportunities. *ACS Photonics* **9**, 3467–3485 (2022).
35. Brasch, V. et al. Photonic chip–based optical frequency comb using soliton Cherenkov radiation. *Science* **351**, 357–360 (2015).
36. Shtyrkova, K. *Fully Integrated CMOS-Compatible Mode-Locked Lasers*. PhD Thesis, MIT (2018).
37. Shtyrkova, K. et al. Integrated CMOS-compatible Q-switched mode-locked lasers at 1900 nm with an on-chip artificial saturable absorber. *Opt. Express* **27**, 3542–3556 (2019).
38. Kärtner, F. X., et al. Integrated CMOS-compatible mode-locked lasers and their optoelectronic applications. In *Proc. IEEE BiCMOS and Compound semiconductor Integrated Circuits and Technology Symposium* (IEEE, 2018).
39. Moreira, R. et al. Optical interconnect for 3D integration of ultra-low loss planar lightwave circuits. *Ad. Photonics* https://doi.org/10.1364/IPRSN.2013.IT2A.4 (2013).
40. Worhoff, K. et al. Reliable low-cost fabrication of low-loss Al_2O_3:Er^{3+} waveguides with 5.4-dB optical gain. *IEEE J. Quantum Electron.* **45**, 454–461 (2009).
41. Purnawirman et al. C- and L-band erbium-doped waveguide lasers with wafer-scale silicon nitride cavities. *Opt. Lett.* **38**, 1760–1762 (2013).
42. Kenyon, J. Erbium in silicon. *Semicond. Sci. Technol.* **20**, R65–R84 (2005).
43. Agazzi, L. et al. Monolithic integration of erbium-doped amplifiers with silicon-on-insulator waveguides. *Opt. Express* **18**, 27703–27711 (2010).
44. Belt, M. & Blumenthal, D. J. High temperature operation of an integrated erbium-doped DBR laser on an ultra-low-loss Si_3N_4 platform. In *Proc. Optical Fiber Communication Conference* (Optica Publishing Group, 2015).

45. Magden, E. S. et al. Monolithically-integrated distributed feedback laser compatible with CMOS processing. *Opt. Express* **25**, 18058–18065 (2017).

46. Li, N. et al. Monolithically integrated erbium-doped tunable laser on a CMOS-compatible silicon photonics platform. *Opt. Express* **26**, 16200–16211 (2018).

47. Rönn, J. et al. Ultra-high on-chip optical gain in erbium-based hybrid slot waveguides. *Nat. Commun.* **10**, 432 (2019).

48. Sun, H. et al. Giant optical gain in a single-crystal erbium chloride silicate nanowire. *Nat. Photonics* **11**, 589–593 (2017).

49. Choudhary, A. et al. A diode-pumped 1.5 μm waveguide laser mode-locked at 6.8 GHz by a quantum dot SESAM. *Laser Phys. Lett.* **10**, 105803 (2013).

50. Choudhury, D. et al. Ultrafast laser inscription: perspectives on future integrated applications. *Laser Photonics Rev.* **8**, 827–846 (2014).

51. Byun, H. et al. Integrated low-jitter 400-MHz femtosecond waveguide laser. *IEEE Photonics Tech. Lett.* **21**, 763–765 (2009).

52. Bradley, J. D. et al. Monolithic erbium- and ytterbium-doped microring lasers on silicon chips. *Opt. Express* **22**, 12226–12237 (2014).

53. van Dalfsen, K. et al. Thulium channel waveguide laser with 1.6 W of output power and ~80% slope efficiency. *Opt. Lett.* **39**, 4380–4383 (2014).

54. Van Emmerik, C. I. et al. Single-layer active-passive Al_2O_3 photonic integration platform. *Opt. Mater. Express* **8**, 3049–3054 (2018).

55. Ahmas, H. et al. 2.08 μm Q switched holmium fiber laser using niobium carbide-polyvinyl alcohol (Nb_2C-PVA) as a saturable absorber. *Opt. Commun.* **490**, 126888 (2021).

56. Ahmad, H. et al. Generation of Q-switched pulses in thulium-doped and thulium/holmium-co-doped fiber lasers using MAX phase (Ti_3AlC_2). *Sci. Rep.* **10**, 9233 (2020).

57. Wang, M. et al. Passively Q-switched thulium-doped fiber laser based on oxygen vacancy MoO_{3-x} saturable absorber. *Opt. Mater. Express* **9**, 4429–4437 (2019).

58. Rahman, M. F. A. et al. Q-switched and mode-locked thulium-doped fiber laser with pure antimony film saturable absorber. *Opt. Commun.* **421**, 99–104 (2018).

59. Latiff, A. A., Rusdi, M. F. M., Hisyam, M. B., Ahmad, H. & Harun, S. W. A generation of 2 μm Q-switched thulium-doped fibre laser based on anatase titanium(IV) oxide film saturable absorber. *J. Mod. Opt.* **64**, 187–190 (2016).

60. Woodward, R. I. et al. Wideband saturable absorption in few-layer molybdenum diselenide ($MoSe_2$) for Q-switching Yb-, Er- and Tm-doped fiber lasers. *Opt. Express* **23**, 20051–20061 (2015).

61. Jung, M. et al. An all fiberized, 1.89-μm Q-switched laser employing carbon nanotube evanescent field interaction. *Laser Phys. Lett.* **9**, 669–673 (2012).

62. Chernysheva, M. et al. High power Q-switched thulium doped fibre laser using carbon nanotube polymer composite saturable absorber. *Sci. Rep.* **6**, 24220 (2016).

63. Liu, J. et al. Graphene-based passively Q-switched 2 μm thulium-doped fiber laser. *Opt. Commun.* **285**, 5319–5322 (2012).

64. Tan, S. et al. Silicon nitride waveguide as a power delivery component for on-chip dielectric laser accelerators. *Opt. Lett.* **44**, 335–338 (2019).

65. Stuart, B. C. et al. Nanosecond to femtosecond laser-induced breakdown in dielectrics. *Phys. Rev. B* **53**, 1749–1761 (1996).

66. Gruzdev, V. in *Laser-Induced Damage in Optical Materials* 1st edn (ed. Ristau, D.) Ch. 4 (CRC Press, 2014).

67. Popa, D. et al. Graphene Q-switched, tunable fiber laser. *Appl. Phys. Lett.* **98**, 073106 (2011).

68. Fou, B. et al. Passively Q-switched Yb-doped all-fiber laser based on Ag nanoplates as saturable absorber. *Nanophotonics* **9**, 3873–3880 (2020).

69. Hussain, S. A. Discovery of several new families of saturable absorbers for ultrashort pulsed laser systems. *Sci. Rep.* **9**, 19910 (2019).

70. Lee, J. et al. Ti_2AlC-based saturable absorber for passive Q-switching of a fiber laser. *Opt. Mater. Express* **9**, 2057 (2019).

71. Woodward, R. I. et al. Tunable Q-switched fiber laser based on saturable edge-state absorption in few-layer molybdenum disulfide (MoS_2). *Opt. Express* **22**, 31113–31122 (2014).

72. Haus, H. A. Parameter ranges for CW passive mode locking. *IEEE J. Quantum. Electron.* **12**, 169–176 (1976).

73. Kärtner, F. X. et al. Control of solid state laser dynamics by semiconductor devices. *Opt. Eng.* **34**, 2024 (1995).

74. Hardy, L. A. et al. Analysis of thulium fiber laser induced bubble dynamics for ablation of kidney stones. *J. Biophotonics* **10**, 1240–1249 (2017).

75. Sherif, A. F. Soft and hard tissue ablation with short-pulse high peak power and continuous thulium-silica fibre lasers. *Lasers Med. Sci.* **18**, 139–147 (2003).

76. Marks, A. J. Laser Lasers in clinical urology: state of the art and new horizons. *World J. Urol.* **25**, 227–233 (2007).

77. Hecht, J. Lidar for self-driving cars. *Opt. Photonics News* **29**, 26–33 (2018).

78. Stephen, M. et al. Integrated micro-photonics for remote earth science sensing (Impress) lidar. In *Proc. IEEE International Geoscience and Remote Sensing Symposium* (IEEE, 2019).

79. Krainak, M. et al. Integrated photonics for NASA applications. In *Proc. Society of Photo-Optical Instrumentation Engineers* (SPIE, 2019).

Methods

Fabrication

The device was fabricated in a silicon photonics foundry (Ligentec) using stepper photolithography on a 100 mm wafer. The standard variation in the SiN thickness and the refractive index was ±5%, and ±0.25%, respectively. The photonic stack consists of a layer of silicon, bottom silicon dioxide, silicon nitride, top silicon dioxide, aluminium oxide and a silicon dioxide cladding layer. The thickness was 230 μm for the silicon substrate, 4 μm for the bottom oxide and 3.3 μm for the top oxide (before the gain deposition). The sidewall angle of the SiN waveguide was 89°. After patterning the SiN layer, an opening is created (by etching away a region of >300-μm-wide top silicon dioxide) on top of the SiN waveguide. The SiN layer and the opening were separated by a thin layer of silicon dioxide of 300 nm thickness (designed value). Fill patterns of SiN were fabricated to maintain a high enough density of SiN (>20%) across the reticle, to avoid fabrication complications. The gain layer was deposited at University of Twente with an RF sputtering tool (Supplementary Information). The chip was mounted in a holder and loaded into an AJA ATC 15000 RF reactive co-sputtering system through a load-lock, then placed on a rotating holder in the main reaction chamber. A 2-inch aluminium target (99.9995% purity) and a thulium target are powered through their own RF sources. A power of 200 W is used on the aluminium target, while 18 W is used on the thulium target that determines the ion concentration in the film. The deposition temperature is around ~400 °C (measured with a thermocouple), and the rate of deposition is around 4–5 nm min^{-1}, amounting to approximately 3 h of deposition. The devices are subsequently protected by a plasma-enhanced chemical vapour deposition (PECVD) silicon dioxide cladding layer. Note that the silicon dioxide cladding layer could be replaced with a CYTOP layer, which is a well-established long-wavelength cladding material[80]. The heaters were fabricated at Aalto University by optical lithography, metal deposition and lift-off, consisting of a 10-nm-thick titanium adhesion layer and 400 nm of gold.

Experiment (*Q*-switching)

In the experiment, the device was optically pumped by an amplified low-noise CW laser (TLG 220; Alnair Labs). We used a high-power polarization-maintaining L-band amplifier (IPG EAR-10-1610-LP-SF). The pump was launched through a half and a quarter waveplate and a 99:1 fibre splitter into a lensed fibre (OZ optics, 3 μm spot size), which was followed by the chip. The pump was monitored with a 1% drop port of the splitter. The coupling to chip loss was measured to be between 2.5 and 3 dB at the pump wavelength, and it was slightly higher than 3 dB at the signal wavelength. The lasing signal was measured with an extended InGaAs integrating sphere photodiode (Thorlab 148 C) and subsequently on the optical spectrum analyser (OSA, Yokogawa AQ6376). The pulses were measured with an extended InGaAs 12 GHz detector (EOT ET 5000 F/APC) and an oscilloscope with a bandwidth of 300 MHz (RS pro RSDS 1304 CFL).

NLI-SA tuning experiment.

To determine the NLI-SA reflectivity curve after fabrication, we coupled a very weak signal at around 1.9 μm from a broadband NKT source (FIU-15). The broadband source was first filtered with a long-pass filter (>1.5 μm) and then a bandpass filter with a 200 nm bandwidth (Thorlab FB 1900-200). The light was coupled into a fibre-based 2-by-2 splitter (3 dB) that was connected to a lensed fibre that launched the light into the NLI-SA of the laser under test (Supplementary Information). The heater on one of the arms of the NLI-SA was tuned using the current, ranging from 0 to 55 mA, over which the resistance varied from 125 to 135 Ω, amounting to a maximum electrical power of ~400 mW. The back-reflected signal was measured through the 3 dB splitter, while care was taken to avoid the collection of signal from facet reflection, which obviously did not change in power

with heater tuning. The peak of the NLI-SA reflectivity curve (Fig. 3) is dependent on the propagation loss in the waveguides (1.8 μm wide), which we estimate, as an upper limit, to be 0.15 dB cm^{-1}, giving >90% reflectivity at the peak. With lower propagation loss, the peak reflectivity increases further (Supplementary Information).

Refractive index. The optical constants of an Al$_2$O$_3$ film were measured by using an ellipsometer with a wavelength span from 240 nm to beyond 11 μm. The refractive index at 1.9 μm was approximately 1.7.

Data availability

All the relevant data supporting this study are available from the corresponding author upon reasonable request.

Code availability

All the relevant computer codes supporting this study are available from the corresponding author upon reasonable request.

References

80. Li, L. et al. Fabrication and characterization of an As$_2$Se$_3$ optical microwire cladded with perfluorinated CYTOP. In *Proc. Conference on Lasers and Electro-Optics* (Optica Publishing Group, 2016).

Author contributions

N.S. conceptualized, designed and tested the laser. J.L. and M.S. helped with testing. K.W. and S.M.G.-B. deposited the gain film on the laser chip. A.C.L. and Z.S. did the heater deposition. H.F., J.C. and M.G. fabricated the chip. S.H. helped in reducing the silica cladding loss. M.A.G. and T.H. discussed the silica cladding loss. H.C.F. and J.D.B.B. helped with film measurements. F.X.K. supervised the project. All authors helped in writing the paper.

Competing interests

The authors declare no competing interests.

Additional information

Supplementary information The online version contains supplementary material available at https://doi.org/10.1038/s41566-024-01388-0.

Correspondence and requests for materials should be addressed to Neetesh Singh.

Peer review information *Nature Photonics* thanks the anonymous reviewer(s) for their contribution to the peer review of this work.

Reprints and permissions information is available at www.nature.com/reprints.